

# Hierarchical Three-Dimensional Microbattery Electrodes Combining Bottom-Up Self-Assembly and Top-Down Micromachining

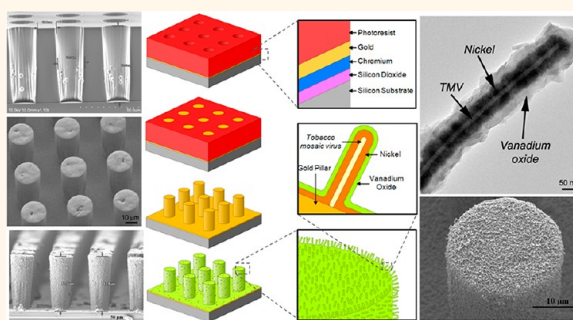
Konstantinos Gerasopoulos,<sup>†,§</sup> Ekaterina Pomerantseva,<sup>‡,§</sup> Matthew McCarthy,<sup>‡</sup> Adam Brown,<sup>||</sup> Chunsheng Wang,<sup>†</sup> James Culver,<sup>||</sup> and Reza Ghodssi<sup>†,‡,§,\*</sup>

<sup>†</sup>Department of Materials Science and Engineering, <sup>‡</sup>Department of Electrical and Computer Engineering, and <sup>§</sup>Institute for Systems Research, University of Maryland, College Park, Maryland, 20742, United States, <sup>‡</sup>Department of Mechanical Engineering and Mechanics, Drexel University, Philadelphia, Pennsylvania 19104, United States, and <sup>||</sup>Department of Plant Sciences and Landscape Architecture and <sup>†</sup>Department of Chemical and Biomolecular Engineering, University of Maryland, College Park, Maryland 20742, United States

The development of novel battery architectures with increased energy and power density is essential for the miniaturization of battery devices for small-scale power applications. Some of these include miniaturization of commercial electronics, development of portable medical devices and implants,<sup>1</sup> as well as efforts toward the widespread use of wireless sensor networks for structural, homeland security, and environmental monitoring.<sup>2</sup> The common denominator in all of these applications is the small overall footprint and compatibility with standard CMOS fabrication that can enable monolithic integration on the same chip. The small footprint requirement limits the available area for the on-board power source and affects battery energy and power density. The fabrication compatibility introduces additional limitations related to the assembly and packaging of the device. These stem from the complexity involved in using traditional battery fabrication and assembly technologies in miniaturized systems. As a result, the development of battery architectures that combine a small footprint with enhanced performance is highly desirable.

Two major research approaches have been pursued for the improvement of battery performance at the micro/nanoscale. The first employs microelectromechanical systems (MEMS) technology and is based on the fabrication of three-dimensional electrode structures. This approach results in increased available surface area and active material loading for the same device footprint. Increased surface area enhances the energy and power density compared to

## ABSTRACT



The realization of next-generation portable electronics and integrated microsystems is directly linked with the development of robust batteries with high energy and power density. Three-dimensional micro- and nanostructured electrodes enhance energy and power through higher surface area and thinner active materials, respectively. Here, we present a novel approach for the fabrication of hierarchical electrodes that combine benefits of both length scales. The electrodes consist of self-assembled, virus-templated nanostructures conformally coating three-dimensional micropillars. Active battery material ( $V_2O_5$ ) is deposited using atomic layer deposition on the hierarchical micro/nanonetwork. Electrochemical characterization of these electrodes indicates a 3-fold increase in energy density compared to nanostructures alone, in agreement with the surface area increase, while maintaining the high power characteristics of nanomaterials. Investigation of capacity scaling for varying active material thickness reveals underlying limitations in nanostructured electrodes and highlights the importance of our method in controlling both energy and power density with structural hierarchy.

**KEYWORDS:** hierarchical · three-dimensional · biotemplating · nanostructures · Tobacco mosaic virus · lithium-ion battery electrodes

traditional 2D thin film batteries.<sup>3</sup> Several electrode designs as well as prototype devices have been proposed in the literature.<sup>4</sup> Some of these include pyrolysis of polymer microstructures,<sup>5,6</sup> electroplating of high aspect ratio metallic electrodes,<sup>7</sup> electrodeposition, spin-casting, vacuum filtration,<sup>8,9</sup> pressure filling,<sup>6</sup> and vapor deposition

\* Address correspondence to ghodssi@umd.edu.

Received for review May 4, 2012 and accepted June 6, 2012.

Published online June 06, 2012  
10.1021/nn301981p

© 2012 American Chemical Society

techniques<sup>10,11</sup> to conformally coat pores formed in silicon or glass substrates. While in these investigations superior energy densities compared to 2D devices have been reported, key challenges still remain. For example, in addition to inherent problems in 3D designs (for example, non-uniform current density distribution<sup>12</sup>), the thickness of the 3D electrode has also been identified as a potential limitation. Since the diffusion pathway is still in the microscale, full lithiation of the active material may not be achieved,<sup>13</sup> limiting the available power density. In addition to their effect on kinetics, thicker electrodes can result in catastrophic failure when chemistries accompanied by huge active material volume expansion are used (for example, silicon).<sup>14</sup> These issues can be addressed by reducing the thickness to the submicrometer range,<sup>1</sup> at the expense of active material mass loading.

A second approach has leveraged on advances in nanotechnology and is aimed at the use of nanostructured materials in battery electrodes. Indeed, nanomaterials have shown significant potential for improving battery performance due to improved properties compared to bulk or microsize particles. These include larger electrode/electrolyte contact area, improved mechanical stability due to the available volume to accommodate structural changes, as well as shorter distances for electron transport and ion diffusion, as has been documented in several reviews.<sup>15–17</sup> These attributes combined can enhance the power density and cyclic stability of the electrodes and address the shortcomings of thicker electrodes. Limitations related to nanostructured materials include the difficulty in synthesis and integration as well as performance concerns such as undesired reactions with the electrolyte.<sup>13</sup> However, the main critical bottleneck in their practical use in micropower sources is the limited energy density. More specifically, the total electrode mass that can be assembled in a given area is low,<sup>4</sup> particularly in cases where nanostructures are grown directly on current collectors.<sup>18,19</sup> Inevitably, even though excellent rate performance and cycle lives can be achieved, the energy density per unit area cannot be easily scaled up accordingly to meet desired levels.

This review of the literature is a clear indication that 3D micro- and nanostructured electrodes independently exhibit advantages for small-scale power applications. However, benefits for one approach are limitation for the other. In this work, we present a new method for the fabrication of three-dimensional microbattery electrodes that combines the advantages of both micro- and nanosized electrodes. The innovating characteristic of our technology is that it utilizes, for the first time, both micro- and nanocomponents in the electrode architecture. This is accomplished by integrating bottom-up nanostructure self-assembly with top-down microfabrication processes in a unique

design. The active battery material is a thin film conformally deposited on a three-dimensional nanoforest scaffold grown on three-dimensional microstructures. This hierarchy in the electrode design has two distinct benefits. First, using the nanostructure approach, active battery material thickness is kept in the nanometer range, which enhances rate performance and power density. Second, the microstructures enable further increase in the total surface area and mass loading, which increases the energy density.

A key enabling technology in this process is the use of the Tobacco mosaic virus (TMV) as a template for the synthesis of nanostructured materials. The TMV is a cylindrical plant virus (300 nm long, 18 nm in diameter) which can be genetically modified with cysteine residues (amino acids with thiol groups) that facilitate electroless metal coating and self-assembly onto various surfaces,<sup>20,21</sup> due to the enhanced metal binding properties of thiols. The metallic thin film encasing the virus is uniform and highly conductive and enhances the rigidity of the resulting 3D nanonetwork. In previous work, we have combined the self-assembled metallized TMV with thin film deposition techniques such as sputtering, electrodeposition, and atomic layer deposition (ALD) to synthesize core/shell Li-ion battery electrodes including Si, TiO<sub>2</sub>, and V<sub>2</sub>O<sub>5</sub>.<sup>22–25</sup> that do not require binders and other conductive additives. In addition to material synthesis, the robustness and self-assembly of the TMV template allows facile integration with microfabrication processes such as photolithographic patterning and coating of 3D geometries fabricated in silicon and other materials.<sup>26</sup> The self-assembly and patterning capabilities are important parameters in our approach. These features are uncharacteristic of other templating methodologies (such as porous membranes), which are planar in nature and can only be combined with 2D current collectors. As a result, further increase in surface area and mass loading can be achieved by utilizing the out-of-plane dimension. In addition, they overcome limitations of nanotube-based micro/nanoforest hierarchical designs that are substrate/catalyst specific.<sup>17,27,28</sup> Consequently, they enable fabrication on substrates with various topologies that can also be compatible with standard semiconductor processes. In this first generation of electrodes, the microstructures were fabricated by electroplating gold micropillars with a moderate aspect ratio of ~3:1 to demonstrate the merits of this technology. This geometry was chosen due to its relatively simpler fabrication. As shown in previous work, however, higher aspect ratios with excellent uniformity can also be achieved.<sup>26</sup> TMV was self-assembled and metallized on the micropillars, and V<sub>2</sub>O<sub>5</sub> was deposited as the active battery material using ALD. V<sub>2</sub>O<sub>5</sub> was selected due to its stability on the TMV template<sup>25</sup> as well as the exceptional suitability of ALD to conformally coat complex three-dimensional

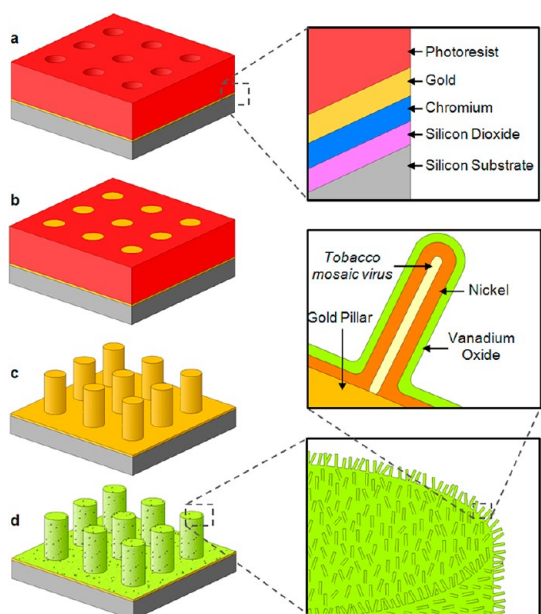


**Figure 1.** Schematic representation of the hierarchical electrode fabrication. (a) Photoresist mold is patterned on the silicon wafer (the inset shows the full layer structures); (b) gold is electroplated through the mold; (c) mold is dissolved in an acetone bath; (d) TMV self-assembles onto the chip surface and then is coated with Ni in an electroless plating solution followed by ALD of  $V_2O_5$ . Insets show the textured micro/nanostructure of the electrode and an individual viral nanorod.

architectures.<sup>29</sup> Recently, ALD of  $V_2O_5$  on highly conductive nanowires has been used in a similar fashion for supercapacitor electrodes.<sup>30,31</sup> Electrodes with and without micropillars were tested to investigate the energy capacity increase in the hierarchical design at various current densities and rates as well as different thicknesses of active materials.

## RESULTS

**Hierarchical Electrode Fabrication.** The hierarchical electrodes consist of arrays of gold micropillars that are coated with the virus-structured nanomaterials. Gold was selected as the material of choice for the micropillars due to the excellent TMV attachment properties as well as its electrochemical inertness in the voltage range of interest. A conceptual schematic of the process is shown in Figure 1. The electrodes were fabricated on 4 in. silicon wafers covered with a thin  $SiO_2$  film. Layers of Cr (20 nm) and Au (250 nm) were deposited using e-beam evaporation to form the adhesion and seed layers, respectively, for the micropillar electrodeposition. A thick positive photoresist (AZ 9260) was used as the electroplating mold, due to the relative simplicity in forming the mold and removing it after deposition using an acetone bath. The photoresist thickness was 60  $\mu m$ , defined by a modified three-spin process,<sup>32</sup> while the hole diameter and pitch size (center-to-center spacing) were 20 and 40  $\mu m$ , respectively (Figure 1a). The dimensions in this

first prototype design were selected based on previous work on the transparency and aspect ratio capabilities of the AZ 9260 resist.<sup>32</sup> The lithographic parameters for the AZ 9260 three-spin process are listed in detail in the Methods section. After lithography, gold was electroplated from a gold sulfite plating solution at pH 7, using a niobium-clad platinum mesh as a counter electrode (Figure 1b). Following electrodeposition, the photoresist mold was removed using sonication in an acetone bath and the wafers were diced into 10.5 mm  $\times$  10.5 mm chips, with an area of 1 cm<sup>2</sup> covered by micropillars (Figure 1c). For comparison, planar chips consisting only of chrome/gold layers (without micropillars) with an identical footprint were also prepared.

TMV self-assembly and nickel coating on the gold micropillars was performed using the general three-step process previously described by our group.<sup>20,21</sup> Coating 3D microstructures, however, is not as straightforward as that for planar surfaces due to the complex topography and the higher aspect ratios involved. Factors such as surface wettability, concentration gradients, and diffusion have to be taken into consideration.<sup>26</sup> Consequently, modifications were made to this general process to facilitate conformal coating of the dense electrode array (details are given in the Methods section). Briefly, the process consists of immersing the chips in a TMV-containing phosphate buffer solution which allows the virus to self-assemble on the gold surfaces, followed by palladium catalyst activation on the surface-exposed viral protein sites and nickel deposition in an electroless plating solution. After nickel coating, the  $V_2O_5$  active material was deposited using ALD at 170 °C with vanadium triisopropoxide and ozone as the vanadium precursor and oxidizing source, respectively<sup>29</sup> (Figure 1d). This process has been found to produce films with high crystallinity after deposition, as indicated by XRD analysis shown in the Supporting Information (Figure S1). As a result, no further annealing of the structures is required.  $V_2O_5$  films with different thicknesses were deposited, as defined by the number of ALD cycles. Here, 1000, 2000, and 4000 ALD cycles were used, expected to produce thicknesses of 30, 60, and 120 nm, respectively.

Figures 2 and 3 show SEM and TEM images of the hierarchical electrode micro- and nanostructure. Very uniform TMV coating of gold micropillars is observed in Figure 2a–c, which contain orthogonal and side views of the hierarchical electrodes. Such uniform coating is a result of the liquid suspension-based TMV attachment (*i.e.*, surfaces that are in contact with the liquid will be coated with TMV) as well as the strong bonds between the TMV and the substrate, enabled by the thiol–gold interactions. These features underline the significance of the TMV approach compared to other nanomaterials' synthetic methods that cannot be easily scaled up to 3D geometries. A close-up view of the top of the micropillar (Figure 2d) shows the highly porous area formed by the three-dimensional virus nanonetwork.

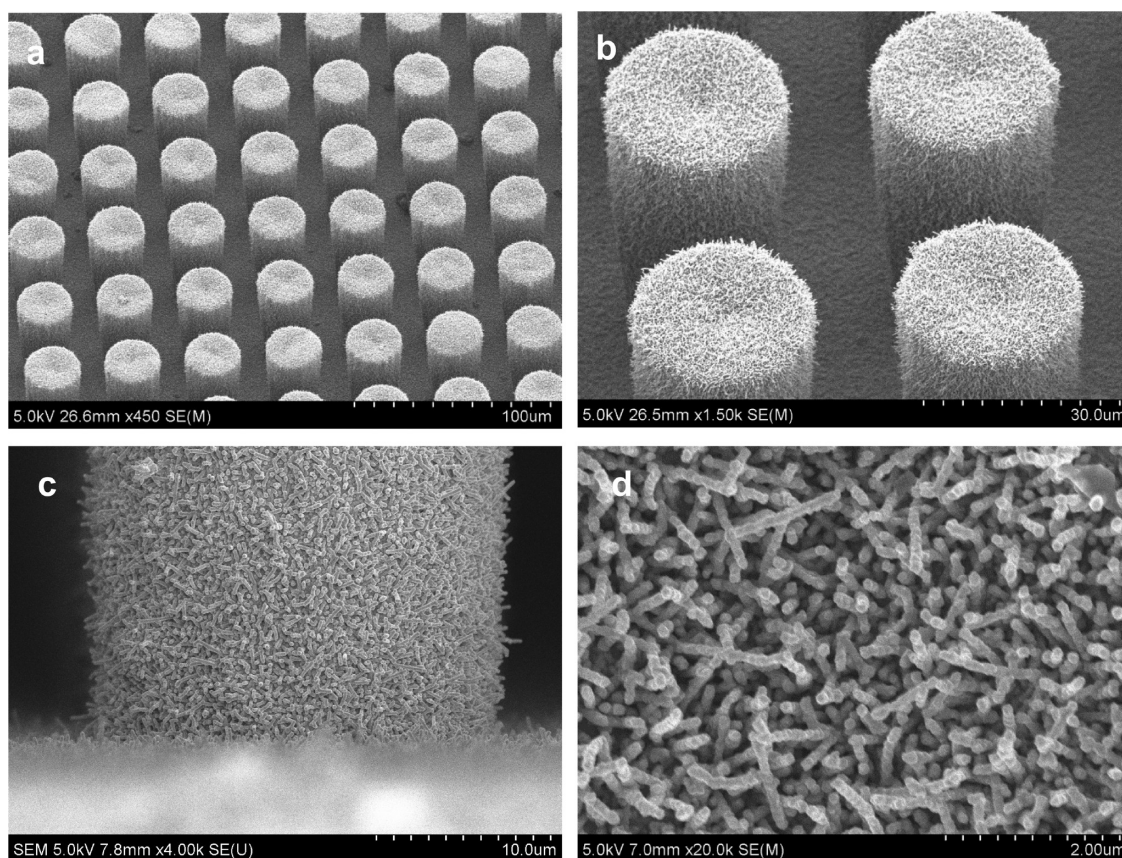


**Figure 2.** SEM images of the hierarchical electrodes. (a–c) Micropillars coated with the TMV/Ni/V<sub>2</sub>O<sub>5</sub> layers at different magnifications (V<sub>2</sub>O<sub>5</sub> was deposited for 1000 ALD cycles); (d) close-up image showing the top of one such micropillar.

Figure 3a shows a cross-section TEM image of an individual viral nanorod with 1000 ALD cycles of V<sub>2</sub>O<sub>5</sub> deposited. The distinct Ni and V<sub>2</sub>O<sub>5</sub> layers encasing the whole TMV rod can be identified. The thickness of the V<sub>2</sub>O<sub>5</sub> film is approximately 30 nm, in close agreement with the expected value estimated by the growth rate.<sup>29</sup> A similar cross-section TEM for 2000 cycles of ALD with its corresponding EDS signal for a line scan across a particle is shown in the Supporting Information (Figure S2), verifying the presence of the V<sub>2</sub>O<sub>5</sub> along the Ni core. In addition to an individual TMV particle, cross-sectional TEM images were taken from the sidewalls of micropillars that were mechanically scraped off the substrate for TEM analysis. Figure 3b shows the electrode nanostructure at the sidewall of the pillar, and it can be observed that the V<sub>2</sub>O<sub>5</sub> coating is uniform regardless of the orientation of the particle. This is a significant attribute of ALD, which is ideally suited to create uniform, conformal coatings of complex 3D geometries with precise control over film thickness.

**Surface Area and Mass Loading Increase.** In order to estimate the expected increase in surface area added by the micropillars, top-view and cross-sectional SEM images were taken as well to evaluate the diameter and height of the electrodes. Characteristic SEM images are shown in Figure S3 in the Supporting

Information. Examination of various samples revealed height variation between approximately 55 and 60 μm, while a variation in the diameter of the pillar across this height was also observed (ranging from roughly 21–22 to 27–28 μm from bottom to top). This diameter variation is attributed to the nonvertical sidewalls formed during photolithography, which is typical in thick positive photoresists.<sup>32</sup>

The increase in surface area  $A$  induced by the micropillars for a cylindrical pattern can be calculated if a unit cell of side  $s$  is drawn from the centers of four adjacent pillars (where  $s$  is the center-to-center spacing). Then the ratio of surface areas with and without pillars for this unit cell gives the increase in surface area, which is described by the following equation:<sup>33</sup>

$$A = \frac{\pi dh}{s^2} + 1 \quad (1)$$

where  $d$  and  $h$  are the diameter and height of the micropillars, respectively. The theoretically expected gain in surface area extracted by the design parameters ( $d = 20 \mu\text{m}$ ,  $h = 60 \mu\text{m}$ ,  $s = 40 \mu\text{m}$ ) is 3.35. On the basis of the fabrication results on the range of heights and diameters measured with SEM characterization, the gain is estimated to be between 3.4 and 4.2. The actual mass loading increase corresponding to this areal gain was calculated by depositing V<sub>2</sub>O<sub>5</sub> for

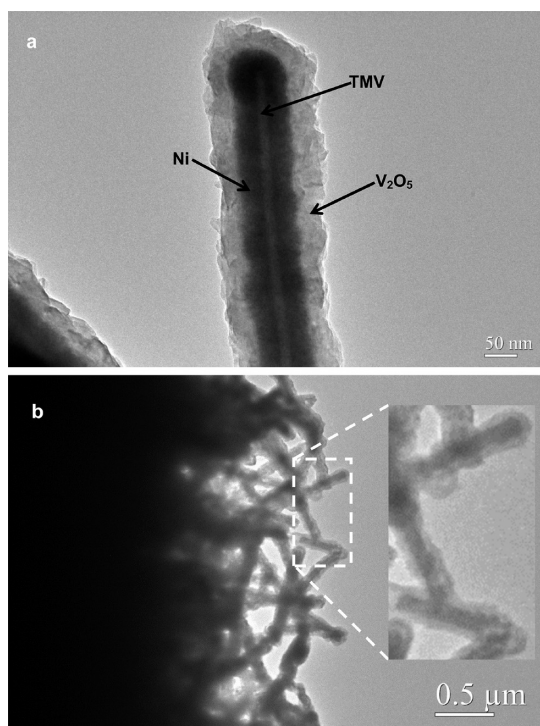


**Figure 3.** Cross-section TEM images of the nanostructures and hierarchical surfaces. (a) Image of an individual virus-templated nanorod showing the distinct layers of TMV, Ni, and  $V_2O_5$ ; the  $V_2O_5$  thickness is approximately 30 nm, in close agreement with the expected value for 1000 ALD cycles; (b) image obtained from the sidewall of a micropillar, showing excellent  $V_2O_5$  coverage for particles regardless of their orientation.

1000 ALD cycles and measuring the mass difference for various sample types before and after ALD deposition. As shown in Figure 3, ALD produces uniform thin coatings across the entire micro/nanogeometry, which implies that the added mass will be proportional to the increase in surface area. The bar graph in Figure 4 plots the average added mass after 1000 ALD cycles of  $V_2O_5$  for four types of samples: flat gold-coated silicon substrates, substrates with micropillars, substrates with virus structures only (denoted nanostructured only), and samples with both micropillars and viral nanostructures (denoted hierarchical). The measurements show average added mass of 13  $\mu\text{g}$  for flat substrates, 41  $\mu\text{g}$  for substrates with micropillars only, 97  $\mu\text{g}$  for nanostructured only substrates, and 296  $\mu\text{g}$  for hierarchical substrates. The larger error bars for samples containing TMV are attributed to some variability in the virus coating uniformity from sample to sample. As indicated previously, the samples used for these experiments were 1.1  $\text{cm}^2$  in area with only 1  $\text{cm}^2$  covered by the micropillars; therefore, this factor should be accounted for in eq 1 to interpret the mass measurement results. Taking this into account, it is observed that the increase in added mass follows the anticipated trend of surface area increase. Specifically, a 3-fold increase in added mass is observed due to the

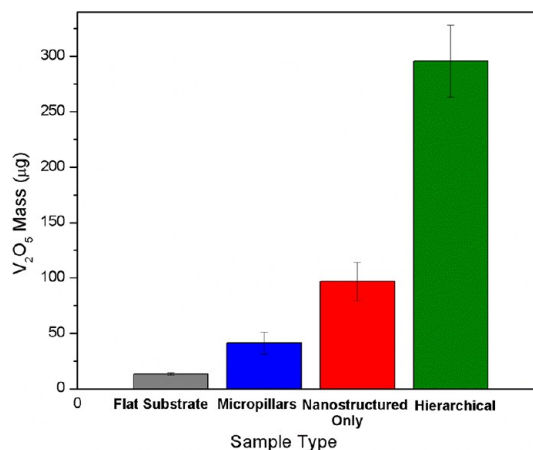


**Figure 4.** Weight measurement results on different samples. Bar graph showing the added mass as measured by microbalance measurement before and after deposition of  $V_2O_5$  for 1000 ALD cycles. The four different sample types that were used are a flat gold-coated Si substrate, a substrate with gold micropillars only, a flat substrate coated with Ni/TMV (nanostructured only), and a sample with both micropillars and Ni/TMV (hierarchical).

micropillars, while a 7.5-fold increase is estimated for virus-structured surfaces. Both of these results are in good agreement with our previous measurements on the virus-induced surface area increase<sup>19</sup> as well as the estimations for the increase in area added by the micropillars in the current work.

**Electrochemical Characterization.** Electrochemical tests were performed in half cell configurations with lithium foil as the counter electrode. The goal was to study the behavior of hierarchical electrodes at various current densities and rates and compare their performance to electrodes with virus-structured electrodes on flat surfaces. The characterization of these half cells can serve as a foundation for future development of full cells based on this hierarchical technology. Specific details about the half cell preparation and testing are provided in the Methods section. In our previous work, the performance of virus-templated  $V_2O_5$  electrodes was compared to flat  $V_2O_5$  films and exhibited an up to 8-fold increase in energy density;<sup>25</sup> consequently, samples without TMV were not tested. The focus of the current work was to investigate the energy density and rate capability characteristics of the three-dimensional electrodes compared to those with nanostructures alone. More specifically, tests were intended to study the scaling of the energy density for the hierarchical electrodes while analyzing the rate performance for different currents. Finally, experiments were performed to analyze the energy density limits of this technology as a function of the active material thickness. It should be noted that capacity values are normalized per unit area ( $\text{cm}^{-2}$ ). This has been identified previously as the primary figure of merit for microbatteries.<sup>3,4</sup> All current parameters, unless otherwise specified, are given in absolute applied values.

Figure 5a shows cyclic voltammetry (CV) scans for electrodes with and without micropillars in the voltage range of 2.6 to 3.6 V, which is a typical voltage range for  $V_2O_5$  cathode cycling. The thickness of  $V_2O_5$  in these experiments was 30 nm (1000 ALD cycles). Two oxidation peaks at 3.35 and 3.15 V as well as two reduction peaks at 3.25 and 3.45 V can be observed for both the hierarchical and nanostructured only electrodes, which are characteristic for lithium insertion in/extraction from the  $V_2O_5$  crystal structure, respectively. It can be seen that the surface area under the curves as well as the peak currents are higher by a factor of 3 for the three-dimensional electrodes. This is in excellent agreement with the increase in mass and surface area. This feature is more clearly illustrated in Figure 5b, which shows discharge/charge curves at a current of  $10 \mu\text{A}$  for these two samples in the same voltage range. The energy storage capacity for the hierarchical electrode is  $38 \mu\text{Ah cm}^{-2}$ , while the nanostructured only electrode exhibits a capacity of  $13 \mu\text{Ah cm}^{-2}$ . On the basis of the mass measurements, the gravimetric capacities for the hierarchical and nanostructured only electrodes are 129 and  $134 \text{ mAh g}^{-1}$ , respectively. These are within the range of the theoretical capacity for  $V_2O_5$  in this voltage window ( $147 \text{ mAh g}^{-1}$ ).<sup>34</sup> As indicated in Figure 5c, where the capacity versus cycle number for the first 35 cycles of operation is plotted, this 3-fold increase in energy density is demonstrated throughout the course of testing. On the basis of the previously reported good stability of  $V_2O_5$  in the selected voltage range and since testing was focused on investigating energy and power density scaling, further cycle stability experiments were not performed and testing was stopped after 35 cycles.

The rate performance and power density of the electrodes were also investigated. We studied the behavior of electrodes with similar  $V_2O_5$  thickness at different loads and current rates. In these studies, half cells were cycled in increments of 10 cycles for progressively increasing current values. Figure 6a shows the average capacities obtained for hierarchical and nanostructured only electrodes for different current densities. The applied currents of 12, 25, 50, and  $100 \mu\text{A}$  correspond to current densities of 11, 22.7, 45.5, and  $91 \mu\text{A cm}^{-2}$ , respectively. The capacities obtained are 3 times higher for the hierarchical electrode for all current densities, indicating that the energy density scales by the same factor, independent of the battery load. A similar trend is also observed when the samples are cycled at similar C rates (it is noted that a rate of  $nC$  means that a battery is fully charged and discharged at  $1/n$  hours). As shown in Figure 6b, the capacity remains 3 times higher for the hierarchical electrodes for all C rates, while both the hierarchical and nanostructured only electrodes demonstrate similar rate capabilities that vary within 2–5% (the rate capability is described in terms of the percentage of capacity retention at each current rate, and it is plotted in Figure S4 in the Supporting Information). This result implies that the

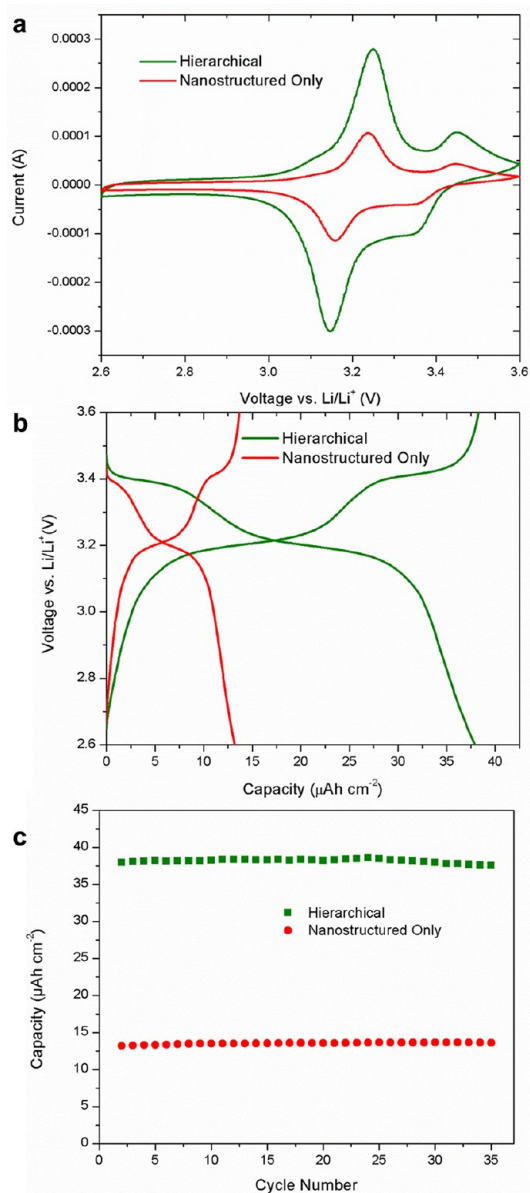


**Figure 5.** Electrochemical characterization of virus-structured electrodes with and without micropillars. (a) Cyclic voltammetry scan in the 2.6 to 3.6 V voltage range at scan rate of 0.5 mV/s for hierarchical and nanostructured only electrodes; (b) galvanostatic charge/discharge curves for hierarchical and nanostructured only electrodes in the same voltage range at an applied current of  $10 \mu\text{A}$  (electrode footprint area was  $1.1 \text{ cm}^2$ ); (c) capacity vs cycle number for the samples used in b for the first 35 cycles of operation.

addition of the micropillars increases the energy density of the electrodes without affecting the high rate performance. This is characteristic of nanostructured materials since higher energy densities are achieved without increasing the thickness of the active material. The energy and power density results combined highlight the merits of the hierarchical fabrication approach.

The effect of increasing active material thickness on hierarchical electrode performance was also investigated. This was performed to identify potential limitations of this

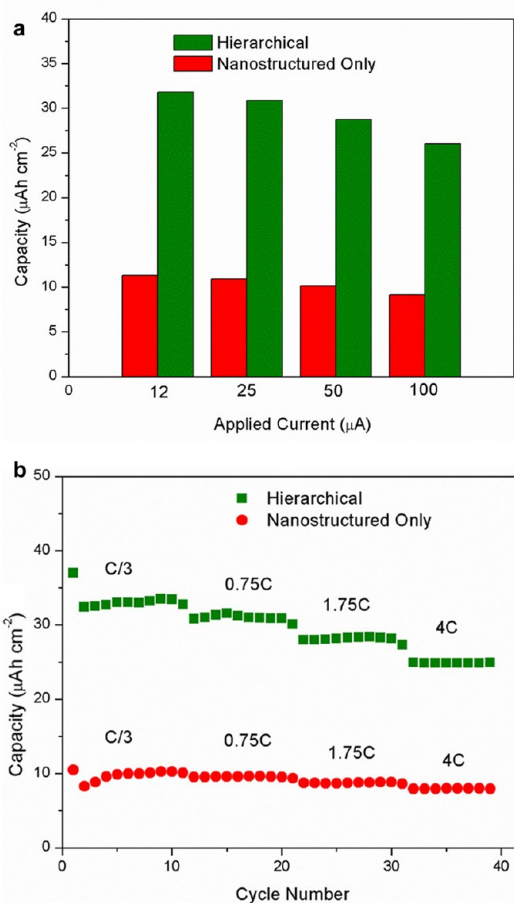


**Figure 6.** Capacity data virus-structured electrodes with and without micropillars at different currents and rates. (a) Average capacities obtained for hierarchical and nanostructured only samples at different currents; the capacities are averaged from 9 cycles at each current value; (b) capacity vs cycle number data for hierarchical and nanostructured only electrodes for the same C rates.

technology in energy density scaling due to gradual loss of the electrode nanostructure.  $V_2O_5$  was deposited on three-dimensional electrodes for 1000, 2000, and 4000 ALD cycles. Characteristic galvanostatic discharge/charge curves for three such samples at a current of  $12 \mu A$  are shown in Figure 7. Capacities of  $33, 63,$  and  $86 \mu Ah cm^{-2}$  are obtained for 1000, 2000, and 4000 cycles of ALD, respectively. Interestingly, the capacity increase exhibits a nonlinearity as the thickness of the active material increases from approximately 60 nm (2000 ALD cycles) to 120 nm (4000 ALD cycles). This behavior, as expected, is closely related to the increase in mass loading, as measured for several samples with different  $V_2O_5$  thicknesses. Figure S5 in the Supporting Information shows the average added mass measurements for these three types of samples that can be used to explain the trend observed in Figure 7. The underlying cause of this behavior can be further understood if the micro/nanostructure of the electrodes is taken into consideration. Figure 8 shows SEM images taken from the top of the micropillars for 1000, 2000, and 4000  $V_2O_5$  ALD cycles.

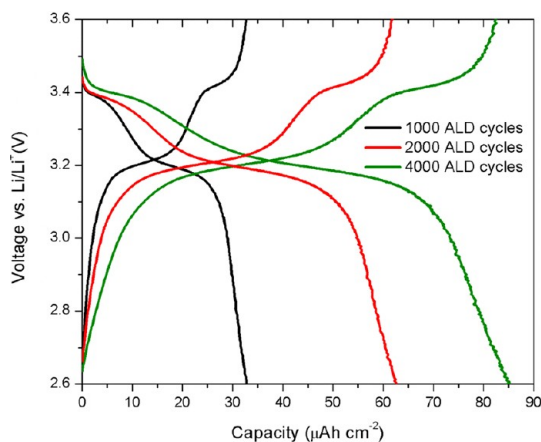


**Figure 7.** Capacities for hierarchical samples with different active material thickness. Galvanostatic discharge/charge curves for hierarchical electrodes at a current of  $12 \mu A$ ;  $V_2O_5$  was deposited for 1000, 2000, and 4000 ALD cycles, aiming at thicknesses of 30, 60, and 120 nm, respectively.

While for thicknesses of up to 60 nm the three-dimensional nanomorphology of the electrodes is maintained, higher active material thickness results in loss of surface area and porosity. Examination of cross-section TEM images taken from hierarchical samples with 2000 and 4000 ALD cycles of  $V_2O_5$  verify the reduced porosity and effective surface area for the thicker active material (Figure 9). This effect is attributed to progressive blocking of open spaces between closely packed adjacent TMV nanorods with increasing deposition thickness. Previously accessible areas are partially planarized, resulting in a nonlinear increase in added material mass.

## DISCUSSION

The hierarchical electrode architecture presented here leverages on two characteristics that are unique to our approach: the self-assembly properties of the TMV (which enable coating of complex geometries) and the robustness of the metalized template (which maintains its 3D shape and can be incorporated into standard microfabrication). Despite the wealth of available nanomaterials synthesis techniques, the aforementioned features cannot be easily accomplished with other methods, limiting their use to planar current collectors or traditional slurry forms. In fact, nanomaterials mixed with binders and conductive additives in a paste (which was then molded into a 3D electrode<sup>7</sup>) constitute the only other example of using nanostructures in microfabricated architectures. Our work, however, is the first demonstration of a three-dimensional electrode that combines two distinct elements in a truly hierarchical geometry, while at the same time experimentally verifying the benefits of each length scale.

The design adopted in this work is based on the use of micropillars as substrates for the assembly of the nanostructured active materials, rather than pores formed in silicon, as shown by other research groups.<sup>10,11</sup> There are two major requirements when pores in silicon

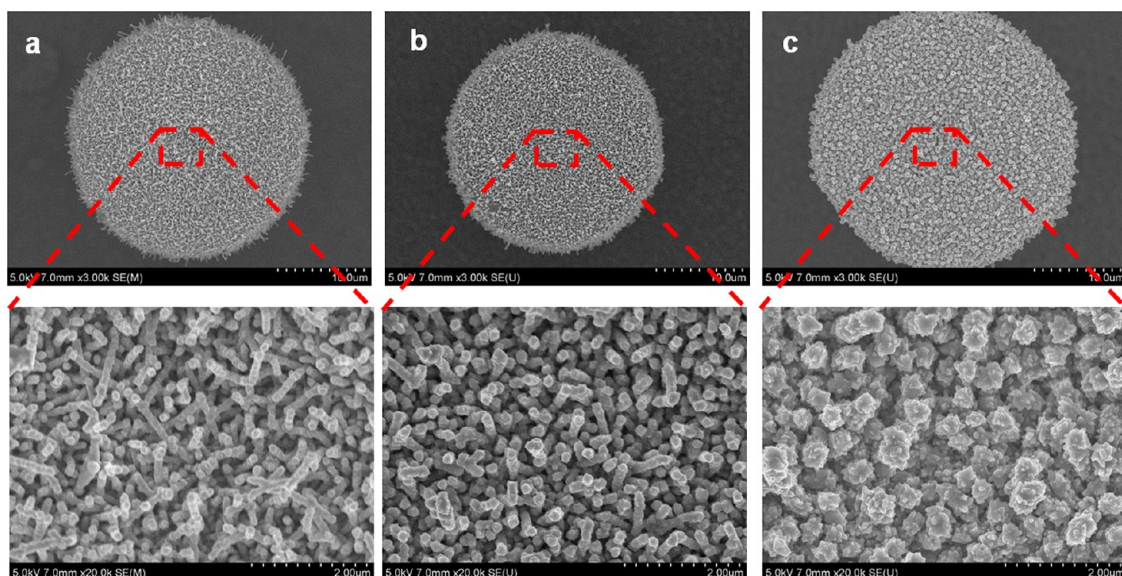


**Figure 8.** Hierarchical electrode morphology for different active material thickness. SEM images showing the top of micropillars for (a) 1000 ALD cycles of  $V_2O_5$ , (b) 2000 ALD cycles of  $V_2O_5$ , and (c) 4000 ALD cycles of  $V_2O_5$ .

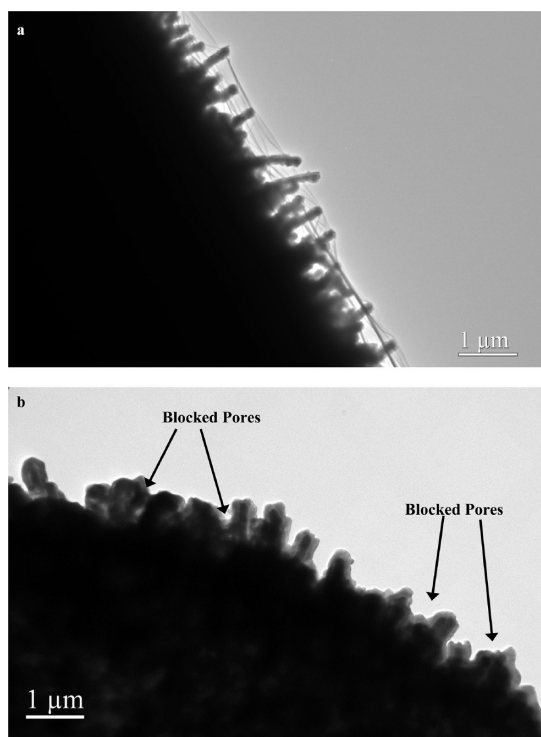


**Figure 9.** Hierarchical electrode morphology for 2000 and 4000 ALD cycles of  $V_2O_5$ . Cross-section TEM images taken from the sidewalls of micropillars for samples with (a) 2000 ALD cycles of  $V_2O_5$  and (b) 4000 ALD cycles of  $V_2O_5$ , showing the porosity of each sample.

are used. The first is the electrochemical isolation of the structural bulk silicon, which dictates the use of a barrier layer. The second is related to the use of suitable methods to conformally deposit the current collector in the high aspect ratio pores. Previously, TiN has served as both the barrier layer and the conductive substrate,<sup>10,11</sup> blocking the silicon from any electrochemical reaction and

enabling electron transport. Due to poor attachment of the TMV on TiN as well as the lack of efficient methods to deposit both barrier layers and current collectors that also promote TMV assembly, other methodologies were explored. Specifically, gold micropillars were selected to form highly conductive 3D current collectors as well as facilitate very uniform viral self-assembly. As in the case of pores in silicon or glass, the micropillars also suffer from “dead volume” since the gold microstructure is not electrochemically active. This can be minimized significantly in future designs by increasing the aspect ratio or using more intricate geometries. One such example is hollow pillars which would be a more desirable architecture as it provides higher surface area with less unusable volume.

While gold is suitable as a current collector for cathodes, similarly, nickel could be used for either anodes or cathodes, while copper micropillars could form the 3D element of anodes. Both materials are significantly cheaper than gold and alleviate any cost concerns involved with the use of gold in practical commercial production. At the same time, active materials can be deposited with various conformal coating deposition techniques, demonstrating the versatility of this approach. This versatility in synthesis and the patterning capabilities of the TMV create tangible opportunities for 3D full cells (microbatteries) based on this technology. Potential designs include interdigitated hierarchical electrodes (leveraging on the photolithographic patterning of TMV) or alternatively sequential deposition of anode, electrolyte, and cathode solid thin films following the protocol presented in the current work.

In this first prototype microbattery electrode architecture, the micropillars were fabricated using a moderate aspect ratio of 2.5:1 to 3:1 to demonstrate the significant merits of this technology. In our previous work, equally

uniform viral coatings of gold-coated silicon-etched microstructures with aspect ratios as high as 9:1 have been accomplished.<sup>26</sup> Consequently, even higher energy density enhancement can be achieved with higher aspect ratio geometries since the nanostructure component of the electrode is based on the TMV self-assembly. As indicated previously, this will significantly improve the volumetric energy density, as well. Even though  $V_2O_5$  was used as a model material, when compared to previously reported data on  $V_2O_5$  electrodes, the capacities obtained from this moderate geometry are comparable to those achieved for nanostructured electrodes or much thicker films.<sup>35,36</sup> More specifically, Nanove *et al.* reported capacities of  $\sim 38$  and  $60 \mu\text{Ah cm}^{-2}$  for RF sputtered 2D electrodes with thicknesses of 1.2 and 1.8  $\mu\text{m}$ , respectively.<sup>35</sup> Similarly, Patrissi *et al.* achieved capacities of  $86 \mu\text{Ah cm}^{-2}$  with  $V_2O_5$  nanofibers (8  $\mu\text{m}$  height, 600 nm diameter) synthesized in modified polycarbonate membranes.<sup>36</sup> In the current work, similar capacities to these nanostructured electrodes were obtained. When compared to the thick films, comparable values with  $V_2O_5$  films as much as 30–40 times thinner (30–60 nm) are reported herein. This was achieved *via* the combination of high surface area nanostructures with three-dimensional micropillars. A significant characteristic of this approach is that further increase in the aspect ratio of micropillars can result in superior energy densities, comparable to values reported for state-of-the-art three-dimensional designs.<sup>7</sup> For example, based on eq 1, electroplating of gold micropillars with similar diameter (20  $\mu\text{m}$ ) through 300  $\mu\text{m}$  silicon wafer molds can result in a surface area gain of 12.8, with a projected capacity of up to  $320 \mu\text{Ah cm}^{-2}$  for a 60 nm  $V_2O_5$  film.

In addition to the structural versatility of this technology, the most significant benefit of the hierarchical approach is highlighted by the effect of increasing active material thickness as discussed in the Results section. It was observed that a nonlinear increase in added mass and energy density was obtained, accompanied by a reduction in surface area and porosity. This might not be too much of a concern for  $V_2O_5$  films that were deposited up to thicknesses of 3–4  $\mu\text{m}$  with little capacity fading at various C rates.<sup>35</sup> However, it can be catastrophic if other battery chemistries are used, based for example on Si or  $\text{TiO}_2$ <sup>22,24</sup> as active materials. These electrochemical systems require high surface area to accommodate volume expansion during lithiation (Si) or store additional lithium at the grain boundaries ( $\text{TiO}_2$ ). In addition to this

functionality, active materials with nanometer thickness are needed to mitigate the effects of poor electronic and ionic conductivity. Consequently, in such electrodes, energy density cannot be effectively enhanced by merely increasing the thickness of the active material, as this may cause cracking and progressive capacity fading (Si) or capacity loss due to reduced surface area ( $\text{TiO}_2$ ). The hierarchical design proposed in this work is ideally suited for the fabrication of high energy and power density microbatteries for such material systems. Using this approach, very high surface area nanostructured materials can be self-assembled onto microstructures. The energy density can be tuned by the microstructures, allowing for thin active materials with highly porous structure.

## CONCLUSION

In summary, the development of three-dimensional microbattery electrodes that consist of micro- and nano-components is presented. The electrodes are made of self-assembled nanostructured forests templated using Tobacco mosaic virus particles, which conformally coat three-dimensional microfabricated gold pillars. The active battery material is  $V_2O_5$ , and it is deposited using atomic layer deposition across the entire micro/nanosurface. Due to the excellent conformality achieved by both the viral self-assembly and the ALD process, the energy density of the three-dimensional electrodes has been increased by a factor that is in good agreement with the expected increase in surface area added by the micropillars. At the same time, thin active material coatings enable fast discharge/charge rates while maintaining higher energy densities. While  $V_2O_5$  was used as a model material, the process can be expanded to a variety of active materials that can be deposited using conformal deposition techniques. The scalability of this approach enables the fabrication of microstructures with higher aspect ratio that can further increase the available energy densities and minimize the “dead volume” from the inactive micropillars. While previous investigations have independently presented the advantages of 3D micro- and nanostructures, the hierarchical electrode in this work is the first demonstration of an architecture that integrates both length scales and combines their respective benefits. Building upon previously demonstrated fabrication capabilities of the TMV template, this technology can serve as the foundation for the development of next-generation energy storage devices with high energy and power densities for small-scale power applications.

## METHODS

**Micropillar Fabrication.** The electroplating mold was fabricated using a three-spin process in positive AZ9260 photoresist. First, hexamethyldisilazane (HMDS) was spun at 3000 rpm for 30 s on the wafer as adhesion promoter. The first AZ9260 layer was spun at 1000 rpm for 40 s, followed by 105 s of soft-baking at

110 °C. Similarly, the second and third layers were spun at 1000 rpm for 50 s and 800 rpm for 60 s and soft-baked at the same temperature for 160 and 300 s, respectively. Between each spin, edge bead removal was performed with EBR solvent at 800 rpm. The wafer was allowed to rehydrate overnight before exposing with a dose of  $2400 \text{ mJ cm}^{-2}$ . Finally, the resist was

developed in a 1:4 AZ400K/DI water mixture for 10 min. After lithography, the wafer was treated with O<sub>2</sub> plasma at 75 W for 60 s to clear any residues from the holes. Before electroplating, an additional treatment with 5% H<sub>2</sub>SO<sub>4</sub> was performed to improve the hydrophilicity of the holes. Electroplating was done at constant current densities of 2 and 4 mA cm<sup>-2</sup> to ensure proper bottom-up deposition without voids for 2.5 and 6.5 h, respectively. The distance between the wafer and the anode was kept at 3 cm, and the bath temperature was set at 30 °C while mechanical agitation from a magnetic stirrer was used to stir the electrolyte solution.

**TMV Coating.** The TMV self-assembly and metallization on flat substrates was performed as previously described.<sup>19,20</sup> This process was modified to ensure conformal coating of the three-dimensional microstructures, based on findings from our previous work.<sup>25</sup> Briefly, chips with micropillars were submerged in a sodium phosphate buffer solution at pH 7, containing TMV at a concentration of 0.2 g L<sup>-1</sup>. The substrates were placed on a rocking platform to assist the diffusion through the dense microstructure matrix and allowed to incubate overnight to maximize TMV assembly. The chips were then immersed in a fresh solution of TMV at 0.1 g L<sup>-1</sup> since in previous work it was observed that mechanical agitation resulted in partial removal of TMV from the top of the microstructures.<sup>25</sup> Next, the substrates were immersed in a solution containing phosphate buffer and sodium tetrachloropalladate (NaPdCl<sub>4</sub>, 98%, Sigma Aldrich, MO, USA) in a 12:1 ratio for 2–3 h. During this stage, the TMV surface was functionalized with Pd nanoclusters. Finally, nickel was deposited from an electroless plating bath. The stock solution (25 mL) was prepared by mixing 0.6 g of nickel chloride (NiCl<sub>2</sub>, 99%, Sigma Aldrich, MO, USA), 0.45 g of glycine (tissue grade, Fischer Scientific, PA, USA), 1.5 g of sodium tetraborate (Na<sub>2</sub>B<sub>4</sub>O<sub>7</sub>, 99%, Sigma Aldrich, MO, USA), and 0.77 g of dimethylamine borane (DMAB, 97%, Sigma Aldrich, MO, USA). This solution was mixed with DI water in a 1:1 ratio, and chips were immersed in the bath for 3–5 min. Nickel is initially deposited onto the Pd catalyzed sites and then the reaction proceeds autocatalytically to form a uniform 20–30 nm Ni coating on the TMV rod. Flat electrodes were coated with this method, as well, and the resulting substrates were compared with samples coated with one overnight TMV step at 0.1 g L<sup>-1</sup>. As expected from previous studies,<sup>19</sup> no significant differences were observed for these samples in terms of both their morphology and their added mass.

**V<sub>2</sub>O<sub>5</sub> Deposition.** The ALD V<sub>2</sub>O<sub>5</sub> process was developed in a BENEQ TFS 500 reactor with a 2 mbar base pressure. VO(OC<sub>3</sub>H<sub>7</sub>)<sub>3</sub> (VTOP) was used as the vanadium precursor, which was kept at 45 °C with a vapor pressure of 0.29 Torr. Ozone served as an oxidizing agent, and it was delivered in the system at room temperature. An MKS O3MEGATM ozone delivery subsystem was employed to supply a stable 18 wt % flow of O<sub>3</sub> from a pure O<sub>2</sub> source. The sequence of pulses used was as follows: 0.5 s VTOP pulse, 1 s N<sub>2</sub> purge, 2 s O<sub>3</sub> pulse, and 1 s N<sub>2</sub> purge. The flow rate of the carrier gas (N<sub>2</sub>) was set at 75–100 sccm, while the flow of O<sub>3</sub> was set at 400 sccm. The deposition rate was measured to be 0.03 nm/cycle (where a cycle denotes one sequence of precursor pulses and purging pulses in the ALD reactor). The V<sub>2</sub>O<sub>5</sub> was deposited for 1000, 2000, and 4000 ALD cycles, aiming at target thicknesses of 30, 60, and 120 nm, respectively. The mass of the active material was determined by weight measurements of the measurements with a high precision microbalance (Mettler Toled, XS105 dualRange, 1 μg) before and after V<sub>2</sub>O<sub>5</sub> deposition.

**Structural Characterization.** The electrode morphology was analyzed using scanning electron microscopy (Hitachi SU-70 HR-SEM). The structural features and composition of the electrode materials were investigated using transmission electron microscopy (JEOL 2100F field emission TEM) with energy-dispersive X-ray spectroscopy (EDS). Phase identification was carried out by X-ray powder diffraction experiments on a Bruker D8 Advance powder diffractometer equipped with LynxEye PSD detector and Ni β-filter using Cu Kα radiation (step size 0.02° in the range of 14° < 2θ < 37°). This range is adequate to identify the main V<sub>2</sub>O<sub>5</sub> peaks while avoiding strong reflections from the Si substrate.

**Electrochemical Characterization.** Electrochemical cells were assembled in standard coin cells (R032). Layers of chrome and gold were sputtered on the backside of the silicon chips before assembly to facilitate the formation of a current collector. The hierarchical and nanostructured only electrodes served as the cathode, lithium foil (Sigma Aldrich, MO, USA) pressed against a stainless steel disk served as the anode, while a Celgard separator (Celgard 3501) was placed between the two electrodes. The electrolyte was a 1 M LiPF<sub>6</sub> solution in ethyl carbonate/diethylcarbonate (EC/DEC, 1:1, Novolyte Technologies, OH, USA). Cell assembly was performed in a glovebox with oxygen concentration of less than 0.2 ppm and argon as the carrier gas. Galvanostatic experiments were performed using a multiple channel battery test station (Arbin Instruments, TX, USA), while cyclic voltammetry scans were obtained using a Gamry G750 series potentiostat (Gamry Instruments, PA, USA), both in the 2.6 to 4 V range.

**Conflict of Interest:** The authors declare no competing financial interest.

**Acknowledgment.** This work was supported by the Laboratory for Physical Sciences (LPS), NSF Nanomanufacturing Program (NSF-CMMI 0927693) and Department of Energy (FG0202ER45975) and the Nanostructures for Electrical Energy Storage, an Energy Frontier Research Center funded by the U.S. Department of Energy, Office of Science, Office of Basic Energy Sciences under Award Number 12DESC0001160. The authors acknowledge the staff at the Maryland Nanocenter and LPS clean-room facilities and Dr. Li-Chung Lai at the Nanoscale Imaging Spectroscopy and Properties Lab for assisting with TEM imaging. Also, Professor Peter Kofinas at the Bioengineering Department at the University of Maryland for granting access to the high precision microbalance.

**Supporting Information Available:** Additional figures. This material is available free of charge via the Internet at <http://pubs.acs.org>.

## REFERENCES AND NOTES

- Notten, P. H. L.; Roozeboom, F.; Niessen, R. A. H.; Baggetto, L. 3-D Integrated All-Solid-State Rechargeable Batteries. *Adv. Mater.* **2007**, *19*, 4564–4567.
- Warneke, B.; Last, M.; Liebowitz, B.; Pister, K. S. J. Smart Dust: Communicating with a Cubic-Millimeter Computer. *Computer* **2001**, *34*, 44–51.
- Long, J. W.; Dunn, B.; Rolison, D. R.; White, H. S. Three-Dimensional Battery Architectures. *Chem. Rev.* **2004**, *104*, 4463–4492.
- Arthur, T. S.; Bates, D. J.; Cirigliano, N.; Johnson, D. C.; Malati, P.; Mosby, J. M.; Perre, E.; Rawls, M. T.; Prieto, A. L.; Dunn, B. Three-Dimensional Electrodes and Battery Architectures. *MRS Bull.* **2011**, *36*, 523–531.
- Wang, C. L.; Taherabadi, L.; Jia, G. Y.; Madou, M.; Yeh, Y. T.; Dunn, B. C-MEMS for the Manufacture of 3D Microbatteries. *Electrochem. Solid State Lett.* **2004**, *7*, A435–A438.
- Min, H. S.; Park, B. Y.; Taherabadi, L.; Wang, C. L.; Yeh, Y.; Zaouk, R.; Madou, M. J.; Dunn, B. Fabrication and Properties of a Carbon/Polypyrrole Three-Dimensional Microbattery. *J. Power Sources* **2008**, *178*, 795–800.
- Chamran, F.; Yeh, Y.; Min, H. S.; Dunn, B.; Kim, C. J. Fabrication of High-Aspect-Ratio Electrode Arrays for Three-Dimensional Microbatteries. *J. Microelectromech. Syst.* **2007**, *16*, 844–852.
- Nathan, M.; Golodnitsky, D.; Yufit, V.; Strauss, E.; Ripenbein, T.; Shechtman, I.; Menkin, S.; Peled, E. Three-Dimensional Thin-Film Li-Ion Microbatteries for Autonomous MEM. *J. Microelectromech. Syst.* **2005**, *14*, 879–885.
- Golodnitsky, D.; Yufit, V.; Nathan, M.; Shechtman, I.; Ripenbein, T.; Strauss, E.; Menkin, S.; Peled, E. Advanced Materials for the 3D Microbattery. *J. Power Sources* **2006**, *153*, 281–287.
- Baggetto, L.; Oudenhoven, J. F. M.; van Dongen, T.; Klootwijk, J. H.; Mulder, M.; Niessen, R. A. H.; de Croon, M. H. J. M.; Notten, P. H. L. On the Electrochemistry of an Anode Stack

- for All-Solid-State 3D-Integrated Batteries. *J. Power Sources* **2009**, *189*, 402–410.
11. Baggetto, L.; Knoop, H. C. M.; Niessen, R. A. H.; Kessels, W. M. M.; Notten, P. H. L. 3D Negative Electrode Stacks for Integrated All-Solid-State Lithium-Ion Microbatteries. *J. Mater. Chem.* **2010**, *20*, 3703–3708.
  12. Hart, R. W.; White, H. S.; Dunn, B.; Rolison, D. R. 3-D Microbatteries. *Electrochem. Commun.* **2003**, *5*, 120–123.
  13. Teixidor, G. T.; Zaouk, R. B.; Park, B. Y.; Madou, M. J. Fabrication and Characterization of Three-Dimensional Carbon Electrodes for Lithium-Ion Batteries. *J. Power Sources* **2008**, *183*, 730–740.
  14. Teki, R.; Datta, M. K.; Krishnan, R.; Parker, T. C.; Lu, T. M.; Kumta, P. N.; Koratkar, N. Nanostructured Silicon Anodes for Lithium Ion Rechargeable Batteries. *Small* **2009**, *5*, 2236–2242.
  15. Bruce, P. G.; Scrosati, B.; Tarascon, J. M. Nanomaterials for Rechargeable Lithium Batteries. *Angew. Chem., Int. Ed.* **2008**, *47*, 2930–2946.
  16. Jiang, C. H.; Hosono, E.; Zhou, H. S. Nanomaterials for Lithium Ion Batteries. *Nano Today* **2006**, *1*, 28–33.
  17. Guo, Y. G.; Hu, J. S.; Wan, L. J. Nanostructured Materials for Electrochemical Energy Conversion and Storage Devices. *Adv. Mater.* **2008**, *20*, 4384.
  18. Cheah, S. K.; Perre, E.; Rooth, M.; Fondell, M.; Harsta, A.; Nyholm, L.; Boman, M.; Gustafsson, T.; Lu, J.; Simon, P.; *et al.* Self-Supported Three-Dimensional Nanoelectrodes for Microbattery Applications. *Nano Lett.* **2009**, *9*, 3230–3233.
  19. Ortiz, G. F.; Hanzu, I.; Djenizian, T.; Lavela, P.; Tirado, J. L.; Knauth, P. Alternative Li-Ion Battery Electrode Based on Self-Organized Titania Nanotubes. *Chem. Mater.* **2009**, *21*, 63–67.
  20. Royston, E.; Ghosh, A.; Kofinas, P.; Harris, M. T.; Culver, J. N. Self-Assembly of Virus-Structured High Surface Area Nanomaterials and Their Application as Battery Electrodes. *Langmuir* **2008**, *24*, 906–912.
  21. Gerasopoulos, K.; McCarthy, M.; Royston, E.; Culver, J. N.; Ghodssi, R. Nanostructured Nickel Electrodes Using the Tobacco Mosaic Virus for Microbattery Applications. *J. Micromech. Microeng.* **2008**, *18*, 104003.
  22. Chen, X. L.; Gerasopoulos, K.; Guo, J. C.; Brown, A.; Wang, C. S.; Ghodssi, R.; Culver, J. N. Virus-Enabled Silicon Anode for Lithium-Ion Batteries. *ACS Nano* **2010**, *4*, 5366–5372.
  23. Chen, X. L.; Gerasopoulos, K.; Guo, J. C.; Brown, A.; Wang, C. S.; Ghodssi, R.; Culver, J. N. A Patterned 3D Silicon Anode Fabricated by Electrodeposition on a Virus-Structured Current Collector. *Adv. Funct. Mater.* **2010**, *21*, 380–387.
  24. Gerasopoulos, K.; Chen, X. L.; Culver, J. N.; Wang, C. S.; Ghodssi, R. Self-Assembled Ni/TiO<sub>2</sub> Nanocomposite Anodes Synthesized via Electroless Plating and Atomic Layer Deposition on Biological Scaffolds. *Chem. Commun.* **2010**, *46*, 7349–7351.
  25. Pomerantseva, E.; Gerasopoulos, K.; Chen, X.; Rubloff, G.; Ghodssi, R. Electrochemical Performance of the Nanostructured Biotemplated V<sub>2</sub>O<sub>5</sub> Cathode for Lithium-Ion Batteries. *J. Power Sources* **2012**, *206*, 282–287.
  26. Gerasopoulos, K.; McCarthy, M.; Banerjee, P.; Fan, X.; Culver, J. N.; Ghodssi, R. Biofabrication Methods for the Patterned Assembly and Synthesis of Viral Nanotemplates. *Nanotechnology* **2010**, *21*, 055304.
  27. Hu, L. B.; Wu, H.; Gao, Y. F.; Cao, A. Y.; Li, H. B.; McDough, J.; Xie, X.; Zhou, M.; Cui, Y. Silicon–Carbon Nanotube Coaxial Sponge as Li-Ion Anodes with High Areal Capacity. *Adv. Energy Mater.* **2011**, *1*, 523–527.
  28. Talapatra, S.; Kar, S.; Pal, S. K.; Vajtai, R.; Ci, L.; Victor, P.; Shaijumon, M. M.; Kaur, S.; Nalamasu, O.; Ajayan, P. M. Direct Growth of Aligned Carbon Nanotubes on Bulk Metals. *Nat. Nanotechnol.* **2006**, *1*, 112–116.
  29. Chen, X.; Pomerantseva, E.; Banerjee, P.; Gregorczyk, K.; Ghodssi, R.; Rubloff, G. Ozone-Based Atomic Layer Deposition of Crystalline V<sub>2</sub>O<sub>5</sub> Films for High Performance Electrochemical Energy Storage. *Chem. Mater.* **2012**, *24*, 1255–1261.
  30. Benson, J.; Boukhalfa, S.; Magasinski, A.; Kvit, A.; Yushin, G. Chemical Vapor Deposition of Aluminum Nanowires on Metal Substrates for Electrical Energy Storage Applications. *ACS Nano* **2012**, *6*, 118–125.
  31. Boukhalfa, S.; Evanoff, K.; Yushin, G. Atomic Layer Deposition of Vanadium Oxide on Carbon Nanotubes for High-Power Supercapacitor Electrodes. *Energy Environ. Sci.* **2012**, *5*, 6872–6879.
  32. Dixit, P.; Tan, C. W.; Xu, L. H.; Lin, N.; Miao, J. M.; Pang, J. H. L.; Backus, P.; Preisser, R. Fabrication and Characterization of Fine Pitch On-Chip Copper Interconnects for Advanced Wafer Level Packaging by a High Aspect Ratio through AZ9260 Resist Electroplating. *J. Micromech. Microeng.* **2007**, *17*, 1078–1086.
  33. Oudenhoven, J. F. M.; Baggetto, L.; Notten, P. H. L. All-Solid-State Lithium-Ion Microbatteries: A Review of Various Three-Dimensional Concepts. *Adv. Energy Mater.* **2011**, *1*, 10–33.
  34. Whittingham, M. S. Lithium Batteries and Cathode Materials. *Chem. Rev.* **2004**, *104*, 4271–4301.
  35. Navone, C.; Pereira-Ramos, J. P.; Baddour-Hadjean, R.; Salot, R. High-Capacity Crystalline V<sub>2</sub>O<sub>5</sub> Thick Films Prepared by RF Sputtering as Positive Electrodes for Rechargeable Lithium Microbatteries. *J. Electrochem. Soc.* **2006**, *153*, A2287–A2293.
  36. Patrissi, C. J.; Martin, C. R. Improving the Volumetric Energy Densities of Nanostructured V<sub>2</sub>O<sub>5</sub> Electrodes Prepared Using the Template Method. *J. Electrochem. Soc.* **2001**, *148*, A1247–A1253.